

Coupling between Gravity Waves and Tropical Convection at Mesoscales

TODD P. LANE

School of Earth Sciences, The University of Melbourne, Melbourne, Victoria, Australia

FUQING ZHANG

Department of Meteorology, The Pennsylvania State University, University Park, Pennsylvania

(Manuscript received 8 June 2010, in final form 12 March 2011)

ABSTRACT

An idealized cloud-system-resolving model simulation is used to examine the coupling between a tropical cloud population and the mesoscale gravity waves that it generates. Spectral analyses of the cloud and gravity wave fields identify a clear signal of coupling between the clouds and a deep tropospheric gravity wave mode with a vertical wavelength that matches the depth of the convection, which is about two-thirds of the tropospheric depth. This vertical wavelength and the period of the waves, defined by a characteristic convective time scale, means that the horizontal wavelength is constrained through the dispersion relation. Indeed, the wave–convection coupling manifests at the appropriate wavelength, with the emergence of quasi-regular cloud-system spacing of order 100 km. It is shown that cloud systems at this spacing achieve a quasi-resonant state, at least for a few convective life cycles. Such regular spacing is a key component of cloud organization and is likely a contributor to the processes controlling the upscale growth of convective systems. Other gravity wave processes are also elucidated, including their apparent role in the maintenance of convective systems by providing a mechanism for renewed convective activity and system longevity.

1. Introduction

Deep convective clouds generate a rich spectrum of gravity waves that have been shown to influence the momentum budget of the troposphere, stratosphere, and mesosphere (e.g., Fritts and Alexander 2003; Kim et al. 2003). In the troposphere, gravity waves generated by clouds help define the mesoscale circulations surrounding those clouds (e.g., Bretherton and Smolarkiewicz 1989; Schmidt and Cotton 1990; Pandya et al. 2000). These circulations can enhance or suppress further convection and become coupled to or feedback on the broader cloud population (e.g., Mapes 1993; Liu and Moncrieff 2004), thereby playing an important role in cloud self-organization. This study examines the coupling between a cloud population and the mesoscale gravity waves it generates in an idealized cloud-system-resolving model.

The coupling between the clouds and the gravity waves they generate formed the basis of wave–conditional

instability of the second kind (CISK) and associated theories (Lindzen 1974; Raymond 1987). These theories sought to explain the propagation of organized convective systems like squall lines using gravity wave arguments, but failed to produce propagation speeds consistent with observations (e.g., Nehrkorn 1986). The coexistence of wave ducting and wave-CISK (the so-called ducted wave-CISK), however, has been successful in explaining the propagation and maintenance of model-simulated organized mesoscale convective bands in the midlatitudes (e.g., Powers and Reed 1993; Koch et al. 2001; Zhang et al. 2001), although some discrepancy exists between their observed and simulated waves. Among other things, this study explores a coupling between clouds and gravity waves in the tropics, which is different from the aforementioned wave-CISK-like mechanisms, and argues that gravity waves help define the preferred horizontal spacing of cloud systems in the population.

Recently, a number of studies have explored the role of gravity waves and inertia–gravity waves in contributing to the formation of propagating regimes of tropical convective organization on a variety of scales. These include large-scale convectively coupled waves (see Kiladis et al. 2009 for a review), clusters and superclusters (e.g.,

Corresponding author address: Todd Lane, School of Earth Sciences, The University of Melbourne, Melbourne VIC 3010, Australia.
E-mail: tplane@unimelb.edu.au

Ouchi 1999; Numaguti and Hayashi 2000; Peng et al. 2001), and organization down to the mesoscale (e.g., Shige and Satomura 2001; Lac et al. 2002; Tulich and Mapes 2008). Many of these studies demonstrate that tropospheric gravity waves play an important role in the initiation of convective systems as they propagate horizontally away from their source. This initiation occurs sequentially, providing the foundation for the propagation of organized systems at speeds faster than storm outflows.

Vertical variations in gravity wave group velocity due to variations in wind speed or stability causes partial or total reflection of upward propagating gravity waves, confining at least some of the wave energy below the reflecting level. Lindzen and Tung (1976) explored a variety of conditions that allow waves to become ducted and showed that a change in stability like that seen at the tropopause can (partially) reflect approximately 33% of the amplitude of hydrostatic waves; depending on the conditions the reflection can be even greater. This partial gravity wave reflection at the tropopause and reflection at the ground underpins the formation of *deep tropospheric gravity wave modes* that possess a vertical structure consistent with the harmonics of the height of the tropopause. The number of antinodes in the vertical are usually used to label these modes; for example, the $n = 2$ mode has a vertical wavelength equal to the tropospheric depth. In reality these modes are not purely sinusoidal owing to vertical variations in shear and stability (e.g., Monserrat and Thorpe 1996; Tulich et al. 2007).

The tropospheric modes have served as the cornerstone of recent arguments pertaining to the role of gravity waves in cloud organization. Mapes (1993) described the processes that lead to the upscale growth of long-lived organized convective systems, such as mesoscale convective complexes (MCCs). Consistent with observations, Mapes represented an MCC as a steady heat source that was a combination of deep heating and stratiform heating, which contains low-level cooling associated with precipitation. He argued that such a forcing would initiate horizontally propagating bores with vertical structures like the tropospheric wave modes. The gravest mode ($n = 1$) would propagate fastest, inducing deep compensating subsidence throughout the depth of the troposphere (see also Bretherton and Smolarkiewicz 1989). On the other hand, the lower-tropospheric cooling associated with precipitation would produce a bore mode with a vertical wavelength equal to the depth of the troposphere ($n = 2$). This $n = 2$ mode induces lower-tropospheric cooling (ascent), which acts to destabilize the area surrounding the MCC, promoting new convection and leading to the upscale growth of the convective system. Fovell (2002) showed that a similar process occurs in the upstream region of long-lived squall lines. Moreover, Liu and Moncrieff

(2004) demonstrated that the earth's rotation acts to reduce the radius of influence of these modes, which leads to more widespread gravity wave effects in the tropics in comparison to the midlatitudes. Finally, Robinson et al. (2008) suggest that resonant convective development occurs when the temporal and spatial scales of the convective forcing are related in a way that is consistent with the gravity wave dispersion relation.

One simplification utilized by Mapes (1993) and other similar studies was the representation of long-lived convective systems as a steady heat source. This assumption is reasonable for long-lived organized systems like MCCs and squall lines but is not representative of short-lived or highly transient mesoscale convective cloud systems. Short-lived clouds produce deep tropospheric wave modes also, and Lane and Reeder (2001) demonstrated that a single convective cloud could have a similar destabilizing influence as a MCC. There is, of course, transience associated with the passage and excitation of the bore modes from a steady source (e.g., Nicholls et al. 1991; Mapes 1993; McAnelly et al. 1997; Shige and Satomura 2000). Yet, the forcing of deep tropospheric modes by a steady source does not allow any preferred horizontal scales to emerge, but a transient heat source allows the modes to have a wavelike structure in the horizontal as well as in the vertical (e.g., Nicholls et al. 1991).

While most previous studies considered the scenario of convection spanning the depth of the troposphere, thereby effectively projecting onto the first two tropospheric modes, Lane and Reeder (2001) demonstrated that shallower convection, like cumulus congestus, would elicit a stronger response from the higher-order $n = 3$ mode. Tulich et al. (2007) also described notable higher-order signals within convectively coupled waves. Similarly, in a multiscale cloud-system-resolving simulation representative of tropical oceanic convection that spanned about two-thirds of the tropospheric depth, Lane and Moncrieff (2008, hereafter LM08) diagnosed notable wave responses from the $n = 1, 2$, and 3 modes. While the depth of the convection is certainly linked to the generation of the wave modes, Holton et al. (2002) showed that the horizontal and temporal characteristics of the source are also crucial for determining the wave spectrum.

The LM08 results also showed a regular spacing of order 100 km for the mesoscale cloud systems in their model simulations (e.g., their Fig. 2b). Such a regular spacing emerges in similar two-dimensional cloud-system-resolving model simulations of multiscale convection (e.g., Shige and Satomura 2001; Liu and Moncrieff 2004). In this study we argue that this regular spacing is the result of a coupling between the convective clouds and the gravity waves they generate. A number of other recent studies also attribute regular convective cloud spacing to

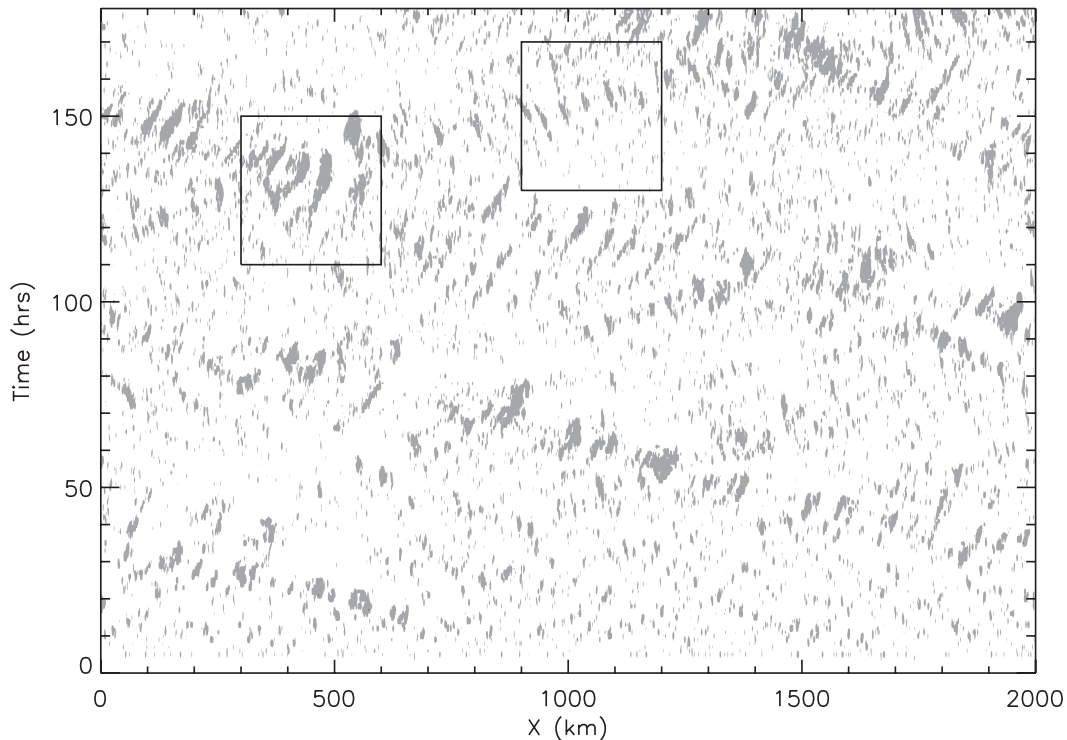


FIG. 1. Time evolution of the 5-km total cloud mixing ratio (cloud water plus ice) in the CSRM simulation; shading represents mixing ratio greater than 0.1 g kg^{-1} . Outlined boxes denote regions of the simulation examined in Fig. 2.

gravity waves. Morcrette et al. (2006) and Marsham and Parker (2006) identified a sequence of bands of convective clouds separated by about 40 km over southern England, and linked the initiation of these bands to gravity waves. Lac et al. (2002) and Halverson et al. (1999) also postulated that observed cloud spacings during the Tropical Ocean and Global Atmosphere Coupled Ocean–Atmosphere Response Experiment (TOGA COARE) case studies were related to gravity waves. Lane et al. (2001) showed regular cloud-system spacing in a three-dimensional cloud model simulation of maritime convection that appeared to be linked to the gravity wave field. Balaji et al. (1993) and Balaji and Clark (1988) also argued that tropospheric gravity waves play a role in defining the cloud spacing of cumulus populations, yet the mechanisms that define the horizontal spacing on the mesoscale remain elusive. Better understanding of these mechanisms could have important consequences for parameterization because such gravity wave–cloud interactions may play a role in adjusting cloud populations toward a more efficient configuration (e.g., Chagnon 2010; Cohen and Craig 2004).

The aim of this study is to explore the coupling between a cloud population and the waves it generates in an idealized cloud-system-resolving model (CSRM). The role of deep tropospheric gravity waves in

contributing to that coupling is the underlying focus, particularly on the mesoscale. The remainder of the paper is organized as follows: section 2 describes an idealized multiscale CSRM simulation of tropical convection, the spectral characteristics of the clouds and gravity waves, the constraints on the gravity wave characteristics, and the processes responsible for the wave–convection coupling. The findings are summarized in section 3.

2. Cloud-system-resolving model simulation

The CSRM simulation examined here was first presented in LM08 and also in Lane and Moncrieff (2010); it is a two-dimensional simulation using the Clark model (Clark 1977; Clark et al. 1996), designed to be representative of weak oceanic tropical convection. The results presented herein utilize a 2000-km-wide periodic domain that is 40 km deep, with 1-km horizontal grid spacing and vertical grid spacing that varies from 50 m near the surface to 200 m farther aloft. The cloud microphysics is treated via a combination of a Kessler (1969) rain scheme and Koenig and Murray (1976) ice parameterization [see Bruintjes et al. (1994) for details of the implementation]. Convection is initiated and maintained with weak surface fluxes and constant

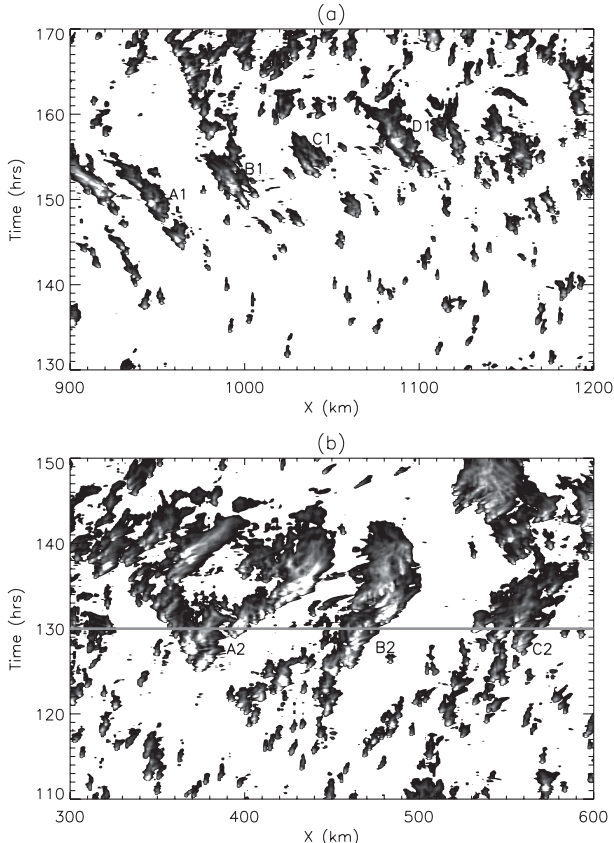


FIG. 2. Total cloud mixing ratio (cloud water plus ice) at 5-km altitude for two different locations and times in the CSRM simulation (marked by boxes in Fig. 1). The threshold for shading (darkest shading) is 0.1 g kg^{-1} and the maximum intensity (lightest shading) is 2 g kg^{-1} . Convective systems described in the text are labeled.

tropospheric cooling, within an environment created from an observed tropical sounding (1330 UTC 26 November 1995, Tiwi Islands, Australia). The cooling is 2 K day^{-1} below 9.5 km and above 9.5 km its magnitude decreases linearly to be zero at 15.5 km . The pertinent feature of this simulation is that clouds are allowed to evolve freely for the 7.5 days of the simulation and the convection has the opportunity to become self-organized. Full details of the simulation, convection, gravity wave fields, and their sensitivity to domain size and model resolution are found in LM08 and Lane and Moncrieff (2010).

a. Emergent scales within the cloud population

Figure 1 shows the space–time evolution of the 5-km total cloud mixing ratio (cloud water plus ice) from the CSRM for the duration of the simulation. This figure demonstrates the development of a variety of regimes of convective organization: short-lived isolated convective

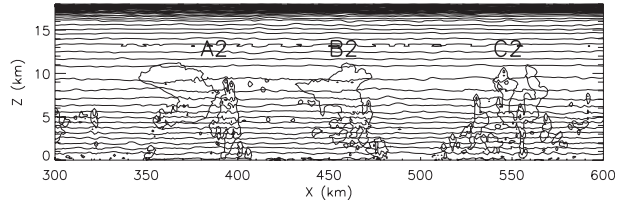


FIG. 3. CSRM simulation results at 130 h (along the line shown in Fig. 2b). Potential temperature contoured at 3-K intervals and contours of the total cloud (cloud water plus ice) mixing ratio at 0.1 g kg^{-1} (thick). Also shown are labels marking the locations of convective systems described in the text.

systems are most prevalent at an early time, and after about 40 h longer-lived propagating systems and clusters of systems emerge. Broad regions of preferential convective activity propagate throughout the domain. For example, an obvious propagating signal begins at the right boundary at approximately 87 h and reaches the left boundary at approximately 145 h; a signal propagating in the opposite direction begins shortly thereafter. Such signals are similar in some respects to larger-scale convectively coupled waves (e.g., Kiladis et al. 2009) but with smaller propagation speeds of approximately $9\text{--}10 \text{ m s}^{-1}$ and are hereafter referred to as *large-scale propagating structures*. The primary focus of this paper is not the large-scale propagating structures (which are unduly constrained by the domain size) but the emergence of a quasi-regular spacing of the mesoscale cloud systems of order 100 km. These regularly spaced cloud systems are present throughout most of the model simulation but are more obvious when they are embedded within the more convectively active regions (i.e., within the large-scale propagating structures).

Two examples of regions and times where the quasi-regular cloud-system spacing is particularly obvious are shown in Fig. 2, indicated as the two regions denoted by boxes in Fig. 1. Figure 2a highlights a group of convective cloud systems that are spaced approximately 50 km apart (A1–D1). These four systems are relatively short-lived, existing for about 3–5 h, and the timing of their development means that they do not all coexist simultaneously. Figure 2b identifies three mesoscale cloud systems that are spaced between 80 and 100 km apart (A2–C2). These three systems are much longer lived than A1–D1, lasting for approximately 10 h. Thus, the quasi-regular cloud spacing can be categorized as mesoscale (meso β). As shown by a cross section through A2–C2 (Fig. 3), most of the deepest clouds only extend to altitudes between 10 and 11 km (well below the tropopause at approximately 16 km), representative of relatively weak oceanic convection.

To further examine the vertical structure of the modeled convection, the microphysical variables are horizontally

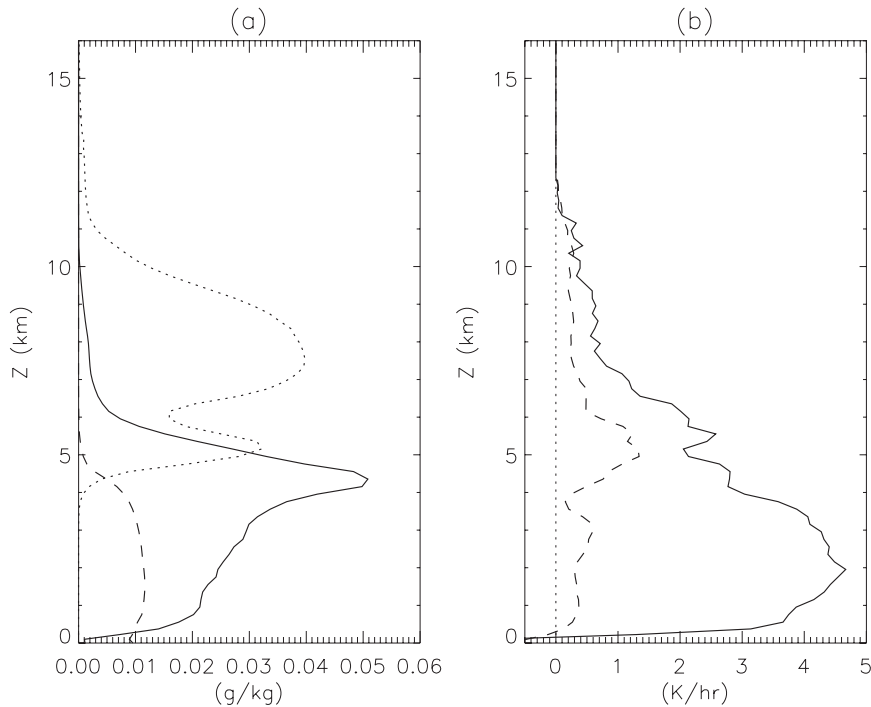


FIG. 4. (a) Vertical profiles of the average mixing ratios of cloud water plus Type-B ice (solid line), Type-A ice (dotted), and rainwater (dashed). (b) Vertical profile of the in-cloud averages of the total rate of change of potential temperature $D\theta/Dt$ (solid), and the total rate of change of potential temperature plus the adiabatic cooling $D\theta/Dt - w\partial\theta/\partial z$ (dashed); both profiles are shown after subtracting the imposed cooling.

and temporally averaged over the entire simulation to construct vertical profiles (Fig. 4a). The relatively simple ice scheme used by the model employs two ice categories; the first category (Type A) encompasses cloud ice, while the second category (Type B) encompasses graupel and snow. With this in mind, Fig. 4a represents a simple separation of rain (rainwater mixing ratio), convective structures (the combination of cloud water mixing ratio and Type-B ice), and anvil regions (Type-A ice). Figure 4a demonstrates that cloud water, graupel, and snow are limited to below 10 km, with minimal cloud ice beyond 11 km. Maximum cloud ice is found at about 8 km, as a result of convective outflows (cf. Fig. 3) and remnant ice clouds after the decay of convective activity. Rainfall is restricted to below 5 km, which is the approximate height of the melting level.

In addition to microphysical variables, Fig. 4b shows the vertical profile of the total rate of change of potential temperature $D\theta/Dt$ (minus the imposed cooling) inside cloud, which is a measure of the diabatic heating. (This profile is constructed from a horizontal and temporal average over the entire simulation and the cloud boundary is defined as the sum of cloud water, ice, and rainwater mixing ratios greater than 0.1 g kg^{-1} .) Consistent with Figs. 3 and 4a, this profile of heating identifies the

uppermost extent of the convection to be approximately 10–11 km. The vertical structure of the heating comprises contributions from shallow and deep clouds and shows notable similarity to observed profiles of the mean heating (e.g., Pessi and Businger 2009). The diabatic heating within clouds is, however, partially offset by the adiabatic cooling $-w\partial\theta/\partial z$ accompanying updraft ascent. The residual heating $D\theta/Dt - w\partial\theta/\partial z$, a quantity related to the Yanai et al. (1973) apparent heat source Q_1 , is also shown in Fig. 4b (minus the imposed cooling). The largest differences between the diabatic heating and the residual heating occur in the lower troposphere where the updrafts are strongest, leading to a peak in the residual heating near 5 km. The uppermost extent of the residual heating is still ~ 11 km. Lane and Reeder (2001) describe how the residual heating may be a better representation of the behavior of the cloud as a gravity wave source, however other nonlinear fluxes have been shown to be important in the wave generation process as well (e.g., Song et al. 2003). Thus, while the simulated convection forms as a response to the imposed cooling that is non-zero below 15.5 km (the tropopause), the simulation has not reached radiative/convective equilibrium and the cloud tops fall well below the tropopause. [It is common for similar simulations to take at least 30 days to reach

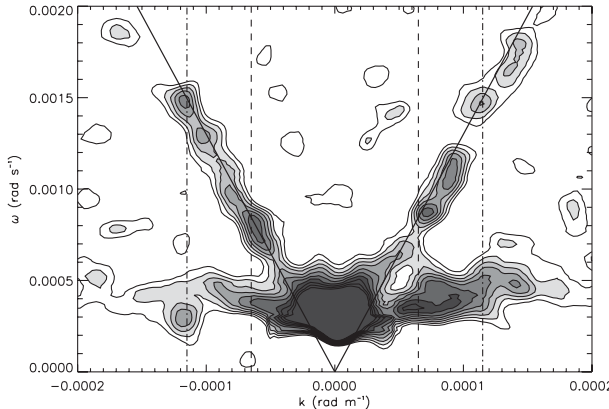


FIG. 5. Power spectrum of the 5-km total cloud mixing ratio divided by a smoothed background spectrum. Contour interval is 0.1, with the smallest contour equal to 1.2; dark shading represents large values. Also shown are solid lines depicting $\omega/k = \pm 13 \text{ m s}^{-1}$, and lines at horizontal wavelengths ($|2\pi/k|$) equal to 55 km (dot-dashed) and 97 km (dashed).

such equilibrium, e.g., Tompkins and Craig (1998); Küpper et al. (2004).] The deepest clouds extend to 10–11 km with precipitation (and implied diabatic cooling) below 5 km.

To better quantify the temporal and spatial characteristics of the cloud population, its spectrum is analyzed using a method similar to Wheeler and Kiladis (1999). First, two-dimensional (frequency–wavenumber) power spectra are calculated for the 5-km total cloud mixing ratio, using every horizontal grid point at 2-min time resolution for two overlapping 100-h time intervals (20–120 and 80–180 h); a single power spectrum is defined using the average of the spectra from these two intervals. (The 5-km cloud is chosen because it identifies the convective cores of deep clouds but is not influenced by anvils that may merge with adjacent clouds at upper levels, which would obscure their underlying spacing.) Similar to Wheeler and Kiladis (1999), the raw cloud spectrum (not shown) is dominated by low frequencies and wavenumbers (i.e., it is “red”), making specific features difficult to identify. To highlight the peaks in the spectrum, it is divided by a “background spectrum,” which is obtained by smoothing the original spectrum over three adjacent frequency and wavenumber bins 10 successive times. The resultant spectrum (referred to hereafter as simply the cloud spectrum) is shown in Fig. 5.

The cloud spectrum (Fig. 5) identifies a number of important signals in the cloud field. Specifically, at time scales shorter than about 3 h ($\omega = 5.8 \times 10^{-4} \text{ rad s}^{-1}$), the peaks follow the lines in frequency–wavenumber space that correspond to $\omega/k = \pm 13 \text{ m s}^{-1}$. These regions of peaked power are approximately symmetric about $k = 0$, with notable sets of peaks at horizontal wavelengths of 55 and

97 km. These sets of peaks occur at periods approximately equal to 70 min ($\omega = 1.5 \times 10^{-3} \text{ rad s}^{-1}$) and 120 min ($\omega = 8.5 \times 10^{-4} \text{ rad s}^{-1}$), respectively. The spectral peaks are at spatial scales larger than individual clouds, reflecting the spacing of mesoscale cloud systems within the population. Here, “cloud systems” refers to longer-lived individual clouds or groups of clouds that persist for multiple convective life cycles. To the extent that the frequency of the spectral peaks represents a characteristic time scale of convective structures embedded within the cloud systems, the peaks correspond to cloud systems spaced approximately 50 km apart (cf. Fig. 2a) with a characteristic time scale of ~ 1 h and cloud systems spaced ~ 100 km apart (cf. Fig. 2b) with a characteristic time scale of ~ 2 h. Finally, accompanying these two notable sets of peaks, there are a number of other identifiable peaks along $\omega/k = \pm 13 \text{ m s}^{-1}$, which highlight the complexity of the mesoscale cloud field and its multiple time scales. Moreover, not all of the peaks along $\omega/k = \pm 13 \text{ m s}^{-1}$ represent the cloud signal at all times during the convective life cycle; the higher frequency peaks are representative of periods of shorter-lived convection (e.g., Fig. 2a) and the lower frequency peaks are representative of periods of longer-lived convection (e.g., Fig. 2b). The other identifiable peaks explain regions of the population with cloud systems of mixed or different longevity to those shown in Fig. 2.

In addition to the peaks in the cloud spectrum along $\omega/k = \pm 13 \text{ m s}^{-1}$ there is significant power at time scales longer than 3 h, which is centered on a period of approximately 5 h ($\omega = 3.5 \times 10^{-4} \text{ rad s}^{-1}$). This peak extends over a broad range of wavenumbers and can be interpreted as representing the lifetime of mesoscale cloud systems. For example, the lifetime of many of the cloud systems in Fig. 1 is at least 5 h. Moreover, this broad peak centered on 5 h contains a number of local maxima that occur at approximately the same horizontal wavelength (viz., 50 and 100 km) as those peaks along $\omega/k = \pm 13 \text{ m s}^{-1}$. Thus, it appears that each emergent horizontal scale composes two time scales: the longer of these time scales likely corresponds to the *mesoscale cloud-system lifetime* and the shorter corresponds to a *characteristic convective time scale*. These two time scales will be discussed later in the paper. Finally, it is important to note that these signals along $\omega/k = \pm 13 \text{ m s}^{-1}$ are not depicting the large-scale propagating structures; these propagate at about $9\text{--}10 \text{ m s}^{-1}$ and are contained within the absolute maximum in the cloud spectrum at low wavenumbers and frequencies.

To explore the cloud patterns and structures associated with the aforementioned peaks in the cloud spectrum, spectral filtering of the 5-km cloud field shown in Fig. 2 is used to isolate some of the important signals. After subtracting the mean, the 5-km cloud field is subjected to

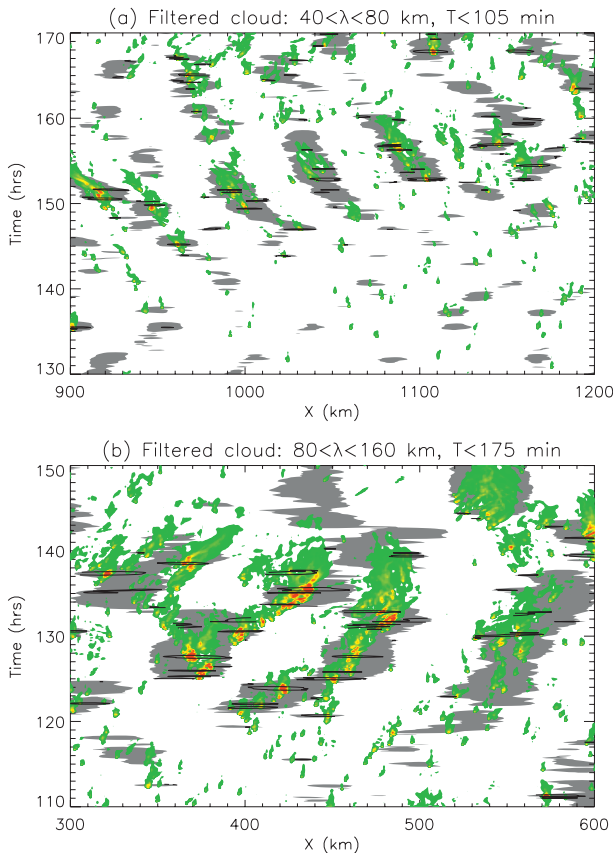


FIG. 6. The 5-km total cloud field as shown in Fig. 2; the threshold for shading (green) is 0.1 g kg^{-1} and the maximum intensity (red) is $\sim 5 \text{ g kg}^{-1}$. Gray shading shows regions where the spatially filtered cloud field, retaining horizontal wavelengths of approximately (a) 40–80 and (b) 80–160 km, exceeds 0.05 g kg^{-1} . Black contours mark the 0.05 g kg^{-1} threshold of the cloud field after the aforementioned spatial filtering and additional temporal filtering, which retains periods less than (a) 105 and (b) 175 min; only contours that overlap gray regions are shown.

two-dimensional (space–time) Fourier analysis to obtain the amplitude spectrum. The filtering is achieved by setting certain spectral components to zero and then performing an inverse transform on the spectrum, which provides the filtered field in physical space. This method is not without some issues; for example, while the filtering is “local” in spectral space it is “nonlocal” in physical space and artifacts of the filtering process can be significant.

Figure 6 shows the unfiltered 5-km cloud field, along with a spatially filtered field (shown in gray) that retains those spectral components (at all frequencies) with horizontal wavenumber magnitudes between (Fig. 6a) 8×10^{-5} and $1.5 \times 10^{-4} \text{ rad m}^{-1}$ (wavelengths between ~ 40 and $\sim 80 \text{ km}$) and (Fig. 6b) 4×10^{-5} and $8 \times 10^{-5} \text{ rad m}^{-1}$ (wavelengths between ~ 80 and $\sim 160 \text{ km}$). These wavenumber ranges were chosen to encompass the aforementioned peaks in the cloud spectrum (Fig. 5) that correspond

to the $\sim 50\text{-km}$ horizontal scale and $\sim 100\text{-km}$ scale evident in Figs. 2a and 2b, respectively. Figure 6 clearly shows that these horizontal scales represent the emergent spatial scales of cloud systems in these regions of the cloud population; the peaks in the filtered field overlay the convectively active regions of the cloud systems and the separation of those peaks defines the cloud-system spacing. The threshold for shading of the filtered field, 0.05 g kg^{-1} , is chosen to best encompass the horizontal extent of the cloud systems in the unfiltered cloud field, that is, the shading does not cover half a wavelength. In each case (Figs. 6a and 6b) the width of the cloud systems is significantly less than half of their spacing.

The spatially filtered cloud field shows temporal variability with periods of a few hours (evident along the edges of the gray shading), along with a longer period modulation exceeding 5 h (i.e., the mesoscale cloud-system lifetime). To further explore the structure of the shorter period variability the spatially filtered cloud field is subject to additional temporal filtering, retaining only those frequencies higher than (Fig. 6a) $1 \times 10^{-3} \text{ rad s}^{-1}$ (periods less than 105 min) and (Fig. 6b) $6 \times 10^{-4} \text{ rad s}^{-1}$ (periods less than 175 min); each case of filtering retains one of the sets of notable peaks in the cloud spectrum that occurs along $\omega/k = \pm 13 \text{ m s}^{-1}$. However, removal of the longer periods eliminates a significant amount of the modulation of the cloud field, resulting in complicated structures everywhere in the domain albeit with the appropriate spatial and temporal scales (a result of the nonlocalness of this filtering). Nonetheless, in almost all regions of active convection in the cloud population these structures form stationary signals due to the superposition of propagating structures (not shown); that is, in regions of active convection the signals do not propagate at $\pm 13 \text{ m s}^{-1}$. Contours of this spatially and temporally filtered spectrum are also shown in Fig. 6 (with black contours), but to simplify interpretation only those contours that coincide with gray shading are shown. The contour threshold (0.05 g kg^{-1}) is chosen to represent the strongest (filtered) signals, and Fig. 6 shows that these contours coincide with most cases of strong convective activity (marked by red shading in the unfiltered cloud field). Thus, this filtering demonstrates that the notable peaks in the cloud spectrum (Fig. 5) corresponding to spatial and temporal scales of (Fig. 6a) 50 km and 1 h and (Fig. 6b) 100 km and 2 h are, indeed, representative of the spatial separation of the cloud systems and the temporal variability at convective time scales.

This additional analysis also highlights that the characteristic convective time scale of 1–2 h identified earlier corresponds closely to the lifetime of individual updrafts embedded within the cloud systems. This 1–2-h time scale is also approximately equal to twice the time it might take

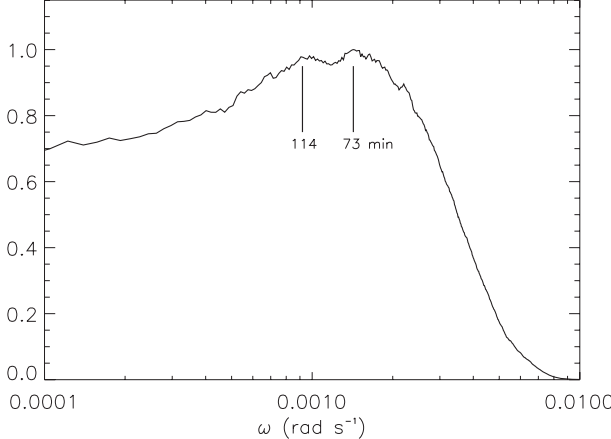


FIG. 7. Spectrum of the 20-km momentum flux vs frequency from the CSRM simulation, normalized by its maximum value. The two largest peaks in the spectrum and their corresponding periods are also marked.

an updraft to span the depth of the cloud; that is, a 5 m s^{-1} updraft would take between 0.5 and 1 h to span a 10-km depth and, so, may also be representative of the largest convective eddy overturn time.

b. Gravity wave characteristics

In this section, the spectra of the gravity waves in the simulation are further examined. The initial focus is on stratospheric wave spectra because they are not contaminated by signals that are not gravity waves (e.g., convective cores). Stratospheric gravity wave spectra of this and similar simulations were discussed extensively by LM08, who showed that the stratospheric gravity wave field was relatively broad, and in horizontal wavenumber space the spectrum was remarkably flat and did not show the dominance of any single horizontal wavelength. Other spectra did, however, identify well-defined peaks. Figure 7 shows the spectrum of momentum flux versus frequency at 20-km altitude, defined using the cospectrum of the horizontal and vertical velocity perturbations. The spectrum is calculated as an average of all of the frequency spectra calculated (from 2-min data) at every horizontal grid point for the two overlapping 100-h time intervals used to create Fig. 5. The momentum flux is chosen for this analysis because it does not unduly emphasize the high or the low frequencies, which have the strongest signatures in the vertical and horizontal velocities, respectively. The frequency spectrum features a reasonably broad maximum centered on $\omega \approx 1.2 \times 10^{-3} \text{ rad s}^{-1}$. While there are a number of local maxima in this spectrum, the two largest are at frequencies equal to 9.2×10^{-4} and $1.43 \times 10^{-3} \text{ rad s}^{-1}$ (periods of 114 and 73 min,

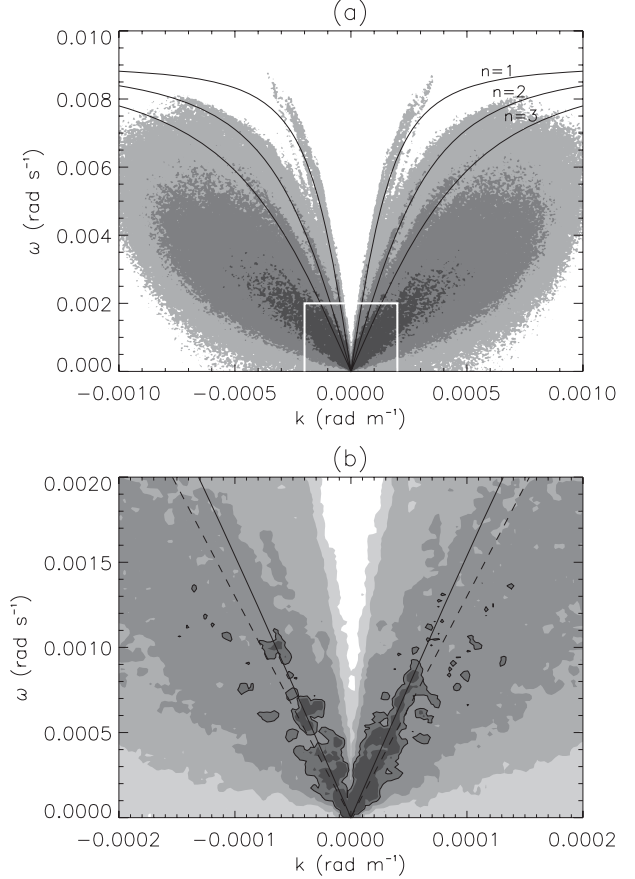


FIG. 8. (a),(b) Two-dimensional spectrum of momentum flux at 20-km altitude, normalized by its maximum value; (b) focus on the frequencies and wavenumbers outlined by the white box in (a). In (a) the three shading levels are equal to 0.0001, 0.001, and 0.01, and lines corresponding to the first three tropospheric modes calculated using the dispersion relation are also shown. In (b) the five shading levels are equal to 0.0001, 0.001, 0.01, 0.04, and 0.06, with 0.04 outlined. Also shown in (b) are lines corresponding to the $n = 3$ mode (solid line) and $\omega/k = \pm 13 \text{ m s}^{-1}$ (dashed).

respectively), which approximately correspond to the two characteristic convective time scales identified in the cloud spectrum (Fig. 5).

The two-dimensional (frequency–horizontal wavenumber) spectrum of momentum flux is shown in Fig. 8. This spectrum is calculated using the same method as in Fig. 5 except it calculates the cospectrum of the horizontal and vertical velocity perturbations at 20 km (unlike the cloud spectrum, it is not divided by a smoothed background spectrum because it is unnecessary for this field). Figure 8a shows the two-dimensional spectrum to be relatively broad but, as discussed by LM08, patterns of local maxima occur along the lines in frequency–wavenumber space that correspond to the deep tropospheric modes. These lines are calculated using the nonhydrostatic dispersion relation for vertical wavelengths of 32 ($n = 1$), 16

($n = 2$), and 10.66 km ($n = 3$), using a value of the Brunt–Väisälä frequency characteristic of the modeled upper troposphere ($9 \times 10^{-3} \text{ rad s}^{-1}$). (Although the frequency–wavenumber spectrum is determined from stratospheric velocities, using the tropospheric Brunt–Väisälä frequency provides an estimate of the tropospheric vertical wavelength at each frequency and horizontal wavenumber; in the stratosphere the vertical wavelengths along these dispersion curves would be approximately half as long, i.e., 16, 8, and 5.33 km.) At the higher frequencies shown in Fig. 8a, the responses corresponding to the $n = 1$, $n = 2$, and $n = 3$ modes are evident, although the $n = 3$ response is located on the edge of the broader maxima. At smaller frequencies and wavenumbers, however, the momentum flux corresponding to the $n = 3$ mode dominates the spectrum (Fig. 8b), with coherent maxima clearly following the $n = 3$ dispersion curve in spectral space. Despite differences in detail, the gravity wave spectrum is mostly symmetric about $k = 0$, with equal wave activity for positive ($k > 0$) and negative ($k < 0$) propagation directions. Thus, while the characteristics of the convective wave source undoubtedly define the shape of the wave spectrum, the height of the tropopause plays an additional role in allowing discrete peaks that match the harmonics of the tropospheric depth to form.

In Fig. 8b the $n = 3$ dispersion curve is nearly exactly linear because at these scales the waves are hydrostatic (the transition to nonhydrostatic waves is depicted in Fig. 8a by the departure of the dispersion curves from being linear). In the hydrostatic limit the horizontal phase speed $c = \omega/k$ of gravity waves is given by $c = N/m$, where N is the Brunt–Väisälä frequency and m is the vertical wavenumber. Hence, the $n = 3$ curve in Fig. 8b, with its 10.66-km vertical wavelength (and assuming $N = 9 \times 10^{-3} \text{ rad s}^{-1}$), corresponds to a horizontal phase speed of approximately 15 m s^{-1} —that is, only slightly faster in magnitude than the $|\omega/k| = 13 \text{ m s}^{-1}$ line in spectral space that the cloud spectrum follows, demonstrating that much of the momentum flux signal overlaps this slightly slower phase speed (Fig. 8b). Thus, at the scales shown in Figs. 5 and 8, the dominant stratospheric gravity wave field approximately coincides with the cloud signal in spectral space that follows $\omega/k = \pm 13 \text{ m s}^{-1}$, suggesting a possible coupling between these processes.

The aforementioned analysis highlights the potential coupling between $n = 3$ gravity waves and the cloud field, which based on Fig. 5 is manifest at two specific time scales (approximately 1 and 2 h). As shown by Lane and Reeder (2001), the vertical velocities (and displacements) associated with the $n = 3$ mode are effective in reducing the convective inhibition and providing preferential locations of convective development because the relevant perturbations are concentrated in

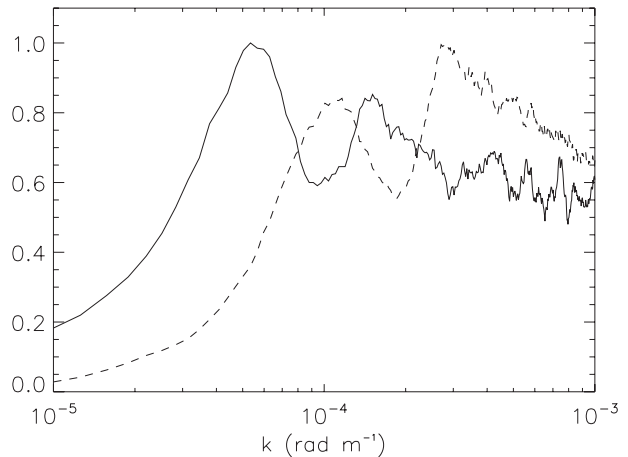


FIG. 9. Normalized amplitude spectra of the vertical velocity at 2.5 km, averaged between periods of 120 and 140 min (solid) and 60 and 80 min (dashed).

the lower troposphere. For the $n = 3$ mode, the first antinode should occur at approximately 2.5 km. To explore the characteristics of the vertical velocity that may play a role in the coupling to the cloud field, the 2.5-km vertical velocity is also analyzed using two-dimensional spectral analysis for the same time intervals as the other spectra. The two-dimensional power spectrum is averaged in frequency space to extract signals corresponding to the two characteristic convective time scales identified in Fig. 5: $\sim 1 \text{ h}$ (averaged between periods of 60 and 80 min) and $\sim 2 \text{ h}$ (averaged between periods of 120 and 140 min). The horizontal wavenumber spectra for those two time scales are shown in Fig. 9. It is important to note that unlike Fig. 8, which shows disturbances in the stratosphere that are predominantly gravity waves, the vertical velocity spectra at 2.5 km contain signals from both gravity wave motion and other processes (e.g., convective updrafts/downdrafts).

Each of the power spectra shown in Fig. 9 contain a similar double-peaked structure. The 120–140-min time-scale spectrum (solid line in Fig. 9) has peaks at horizontal wavenumbers of approximately 1.4×10^{-4} and $0.55 \times 10^{-4} \text{ rad m}^{-1}$ (horizontal wavelengths of 45 and 114 km, respectively). The 60–80-min time-scale spectrum (dashed line in Fig. 9) has peaks at horizontal wavenumbers of approximately 3.0×10^{-4} and $1.1 \times 10^{-4} \text{ rad m}^{-1}$ (horizontal wavelengths of 21 and 57 km, respectively). The longer wavelength peaks of each spectrum correspond to the $n = 3$ signal, with phase speeds between 13 and 15 m s^{-1} , and agree almost exactly with the emergent cloud-system spacing (cf. Fig. 5). On the other hand, the shorter wavelength peaks are related to the width of the cloud systems (i.e., the wavelength is twice the width of the systems). In particular, many shorter-lived

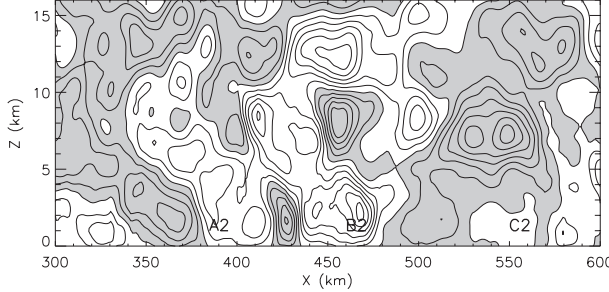


FIG. 10. Vertical velocity from the CSRM at 126 h for the same part of the model domain shown in Fig. 3. The vertical velocity is smoothed (as described in the text): contour interval is 1 cm s^{-1} with negative values shaded. The locations of convective systems marked in Fig. 3 are also shown.

systems (e.g., Fig. 2a) are about 10 km wide and many longer-lived systems (e.g., Fig. 2b) are about 20 km wide. LM08 showed that this shorter scale signal, corresponding to the characteristic time scale and size of individual clouds, dominates the stratospheric phase speed spectrum aloft. Thus, for each characteristic convective time scale, the 2.5-km vertical velocity contains a signal that corresponds to the characteristic width of cloud systems within the population and a signal that matches the emergent spacing of those cloud systems. In the following sections, it will be shown that the convective structures embedded within the cloud systems are responsible for generating the $n = 3$ wave mode, which then becomes coupled to the cloud population.

c. Gravity wave–convection coupling

Spectral analysis of the cloud field, stratospheric gravity waves, and lower-tropospheric vertical velocity all showed the occurrence of the $n = 3$ gravity wave mode that coincides in spectral space with a coherent signal in the cloud field. The deep tropospheric modes can influence convective development through either enhancement or suppression of convective activity, and the local effect depends primarily on the phase of the wave. Both enhancement and suppression are likely to be important for coupling with the cloud population, and for a positive feedback to occur the clouds and the waves would need to become (at least partially) phase locked. Moreover, collocation of signals in spectral space is not necessarily sufficient for coupling to occur; the clouds and the waves also need to be collocated in physical space.

Consider a cross section of the (smoothed) vertical velocity at 126 h (Fig. 10), which is at the same location as Fig. 3. [To create Fig. 10 the vertical velocity is first smoothed in the horizontal over 40 adjacent grid points (40 km) and then smoothed in the vertical over 10 adjacent grid points (2 km), removing the convective-scale

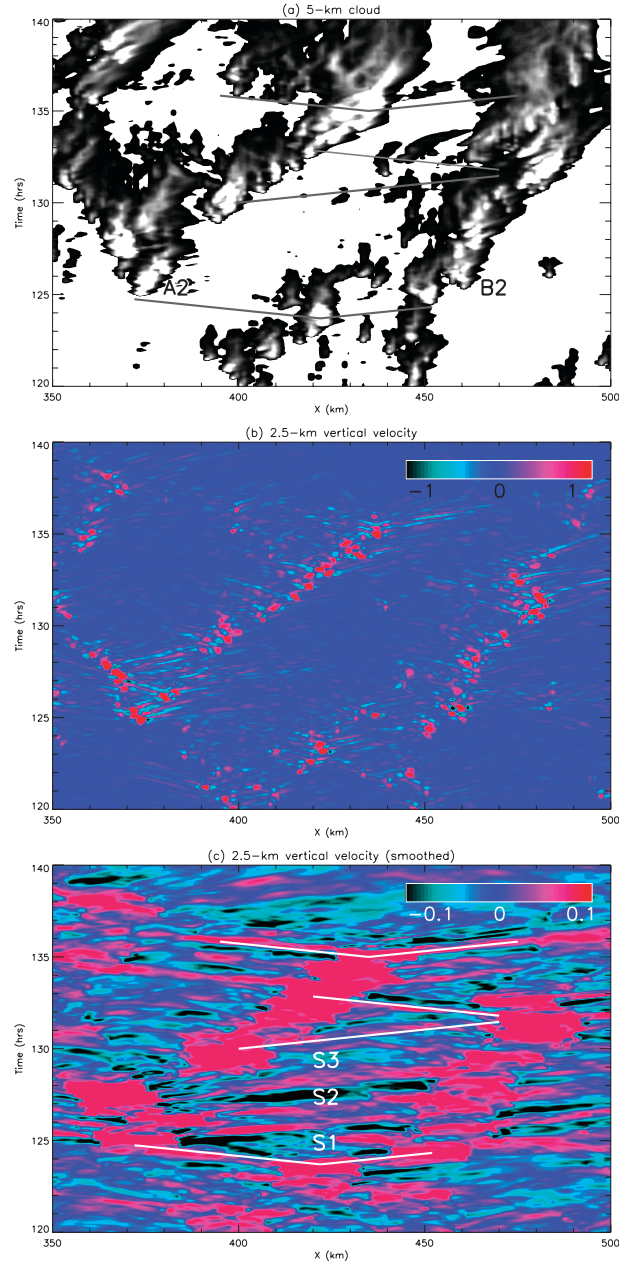


FIG. 11. (a) Total cloud mixing ratio at 5 km for the CSRM simulation (shading as in Fig. 2), (b) 2.5-km vertical velocity (m s^{-1}), and (c) smoothed 2.5-km vertical velocity (m s^{-1}). Lines overlaid on (a) and (c) depict phase speeds of $\pm 13.3 \text{ m s}^{-1}$ and labels on (a) and (c) are discussed in the text.

signals and retaining the phase information of signals with wavelengths larger than the smoothing footprint.] Also labeled in Fig. 10 are the locations of the three convective cells that develop around this time and eventually form into those cloud systems shown in Fig. 3. Figure 10 illustrates that the tropospheric vertical velocity contains many coherent structures consistent with the deep

tropospheric wave modes. As expected, the signals are neither purely sinusoidal in the horizontal nor in the vertical and consist of a variety of other complicated structures. Yet, the $n = 3$ mode is obvious at a number of locations in the figure along with evidence of the $n = 2$ mode as well. The perturbations in the lower troposphere possess maxima at about 2–3-km altitude and half-vertical wavelengths of about 5 km—consistent with the $n = 3$ mode. The horizontal structure of these perturbations is wavelike, with a horizontal wavelength between 70 and 100 km. Importantly, the regions of lower-tropospheric ascent also coincide with the locations of the developing convective cells A2, B2, and C2, with subsidence occurring in between. Thus, at this time, the $n = 3$ gravity waves and the incipient convection are sufficiently in-phase that cooperative feedbacks could occur.

To examine the temporal evolution of the lower-tropospheric signals, time–distance sections of the 5-km cloud, 2.5-km vertical velocity, and 2.5-km smoothed vertical velocity are shown in Fig. 11, focusing specifically on the evolution of cells A2 and B2 (marked in Fig. 11a). The raw vertical velocity (Fig. 11b) is dominated by the highly transient convective cores embedded within the mesoscale cloud systems and the short wavelength gravity waves that emanate from these, which have horizontal wavelengths similar to twice the width of the cores (cf. the shorter wavelength spectral peaks in Fig. 9). The temporal variability of the convective cores also illustrates the characteristic convective time scales of 1–2 h. To focus on the longer wavelength gravity waves, this raw velocity field is smoothed over 20 adjacent grid points (20 km) in the horizontal direction to produce Fig. 11c. The smoothed vertical velocity identifies a complex field of propagating structures that appear to interact with the cloud population. Waves with periods between 1 and 2 h and horizontal phase speeds of approximately 13 m s^{-1} are pronounced [cf. the $n = 3$ mode (Fig. 8b) and the longer wavelength spectral peaks in Fig. 9]. Gravity waves with similar characteristics are generated by each active convective system, regardless of their location in the population.

Figure 11 provides further evidence of coupling between the cloud population and the gravity wave field. As the mesoscale cloud systems spawned by cells A2 and B2 evolve, periodic regions of subsidence occur between the convective systems (e.g., regions labeled S1, S2, and S3) alongside periodic regions of ascent collocated with bursts of convective activity. The period is approximately 2 h and the spacing of these regions of ascent (i.e., the convective cores) is comparable to the horizontal wavelength of the propagating waves. Hence, the waves and the convection become phase locked, achieving a quasi-resonant state. The periodic structures are not

propagating per se, but formed by the interaction of waves propagating in opposite horizontal directions. However, the interaction is not perfect and only lasts for a few periods and is complicated by other wave signals. Yet, similar structures prevail throughout much of Fig. 11c and other regions of the cloud population. Thus, appropriately spaced clouds and the gravity waves that they generate can become resonant; a cloud spacing that matches the preferred horizontal scale of the $n = 3$ tropospheric mode (in this case) facilitates that resonance.

The previous discussion has shown that the horizontal scales that emerge in the CSRM correspond to the horizontal wavelengths of the (horizontally propagating) $n = 3$ tropospheric modes. However, an apparent source of disagreement is that the waves themselves are propagating at about $13\text{--}15 \text{ m s}^{-1}$, whereas the clouds appear to be moving much slower (only a few meters per second, e.g., Fig. 2). This difference between the gravity wave propagation speed and the speed of the convective systems was one of the main disadvantages of wave-CISK-type theories (e.g., Nehrkorn 1986; Raymond 1987). Nonetheless, this disagreement does not necessarily eliminate gravity waves as the underlying mechanism that defines the horizontal scale of the clouds within the population.

First, it is important to note that the signal in the cloud spectrum (Fig. 5), aligned with $\omega/k \approx \pm 13 \text{ m s}^{-1}$, should not be interpreted as the propagation speed of the clouds. (The individual clouds move at only a few meters per second.) Rather, it should be interpreted as the ratio of the separation scale to the characteristic convective time scale. As demonstrated by Fig. 6, the signals at positive and negative wavenumbers interfere to create a stationary, yet transient, signal. Similarly, the symmetric spectrum of gravity waves (Fig. 8) implies similar interference, provided the gravity waves propagating in opposite directions are collocated in physical space. Indeed, Fig. 11c illustrates that standing-wave-like patterns occur in the tropospheric gravity wave field, at least for a few wave periods.

In an unsheared environment, like that considered here, the cloud population generates gravity waves that, on average, show no preferential horizontal direction of propagation (e.g., Fig. 8). The characteristics of the deep tropospheric modes are such that the vertical group velocity is small and will therefore reside in the troposphere for a substantial time and extend large horizontal distances from their source. Thus, in a cloud population with active clouds over an extensive area, the tropospheric wave field will consist of a rich field of waves propagating in all horizontal directions simultaneously: a situation conducive to wave interference. Such interference is facilitated if the gravity waves propagating in opposite directions have similar character; visual inspection of the

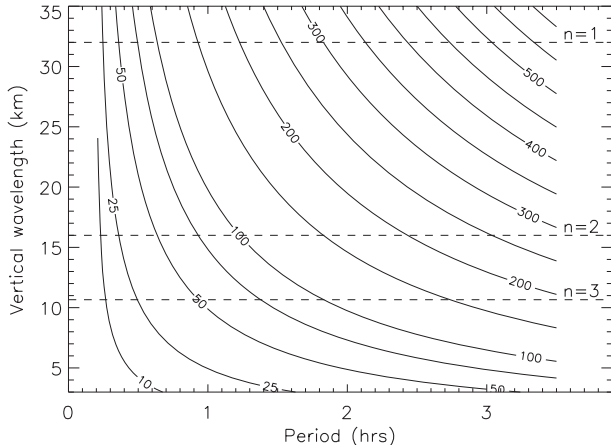


FIG. 12. Horizontal wavelength as a function of wave period and vertical wavelength, derived from the nonhydrostatic dispersion relation assuming that $N = 9 \times 10^{-3} \text{ rad s}^{-1}$. Also shown are the vertical wavelengths corresponding to the first, second, and third tropospheric modes, assuming a tropopause height of 16 km.

wave field (Fig. 11c) confirms that this is true, which will be discussed further in the next subsection.

The coupling between the cloud population and the waves that it generates could eventuate in a number of ways. For example, two (or more) cloud systems could randomly form at the appropriate spacing, facilitating a resonant feedback between the cloud systems and the waves they generate (e.g., Figs. 2b and 11c). A second process might occur in a population of randomly spaced smaller clouds, or cloud systems, with those clouds coinciding with the upward phase of a preexisting gravity wave field experiencing preferential conditions for further development. The development of these “statistically lucky” clouds would feedback on the background wave field, amplifying the signal, and *inter alia* act to further suppress convective development in the downward phase of the gravity waves. Such a process would likely be manifest as the emergence of a preferential spacing in an evolving cloud population (such as in Fig. 2a). A similar hypothesis was presented by Balaji and Clark (1988) and requires the presence of an established wave field, which would exist in an active cloud population like that considered here. It is likely that both processes are at play here, probably in combination in some parts of the population and in isolation in others.

d. Constraints on gravity wave scales

In the previous discussion it was shown that a quasi-regular spacing of simulated cloud systems emerges as a consequence of a coupling to the gravity wave field, which itself must have a well-defined horizontal wavelength (as opposed to being composed of a broad

spectrum). This subsection focuses on the processes that can define the horizontal wavelengths of the deep tropospheric gravity wave modes.

Consider the nonhydrostatic dispersion relation for a two-dimensional gravity wave in a nonrotating frame of reference with no background flow: $\omega^2 = N^2 k^2 / (m^2 + k^2)$, where N is the Brunt–Väisälä frequency and m the vertical wavenumber. This can be rearranged into

$$\lambda_x = \lambda_z \left(\frac{N^2 T^2}{4\pi^2} - 1 \right)^{1/2}, \quad (1)$$

where $\lambda_x = 2\pi/k$ is the horizontal wavelength, $\lambda_z = 2\pi/m$ is the vertical wavelength, and $T = 2\pi/\omega$ the wave period. While clearly just a rearrangement of the dispersion relation, Eq. (1) is pivotal to the discussion herein and simply states that, for a given background stability, wave period, and vertical wavelength, the horizontal wavelength of a propagating linear gravity wave is constrained. The solution to Eq. (1) is shown in Fig. 12, using $N = 9 \times 10^{-3} \text{ rad s}^{-1}$ for a range of vertical wavelengths and periods. This relationship is essentially the same as that presented by Lindzen and Tung (1976), who discussed how the length scale could be determined from a characteristic time scale and the wave phase speed (which is directly proportional to the vertical wavelength of hydrostatic waves). Nevertheless, the germane issue here is that a fixed horizontal wavelength occurs if the period and vertical wavelengths are defined in some way by the flow.

The height of the tropopause is the first important scale to be considered because it defines the depth of the tropospheric modes, which are notable features of the wave spectrum (e.g., Fig. 8). This depth also poses an uppermost limit on the depth of deep convection, although this limit is of secondary importance to the discussion herein. In this simulation (and much of the tropics), the tropopause is 16 km high and the vertical wavelengths of the $n = 1, 2$, and 3 modes are 32, 16, and 10.66 km, respectively. While the convection generates a broad spectrum of gravity waves, those waves that project onto the tropospheric wave modes reside in the troposphere for a significant time and make an important contribution to the tropospheric gravity wave spectra and coupling to the cloud population. Moreover, the depth of the troposphere will vary minimally over the cloud population, causing minimal horizontal variations in the depth of the tropospheric modes (although changes in stability accompanying convection could vary their vertical structure considerably).

Now consider the processes that define the wave period. In a linear system, Holton et al. (2002) showed that a periodic (in time) forcing generates gravity waves with frequencies equal to the source frequency; in a steady

background flow the wave frequency is conserved following a ray (Bretherton 1966). Therefore, a gravity wave field with a well-defined period could be caused by a periodic wave source, forced by an impulsive source with the appropriate characteristic time scale, or parameterized by a periodic source. The CSRM shows that the gravity waves have a frequency spectrum with two well-defined peaks at periods of about 1 and 2 h (Fig. 7). The cloud spectrum (Fig. 5) also identifies the emergence of discrete peaks at similar periods, namely, the so-called characteristic convective time scales. Indeed, the convective cells embedded within the mesoscale cloud systems are quasi-periodic, with periods from 1 to 2 h (Fig. 11b). Accordingly, the gravity waves emitted by those convective cells have periods from 1 to 2 h (Figs. 11b and 11c). This characteristic convective time scale will depend on the thermodynamic conditions of the cloud environment, including the depth of the convection, its intensity, and the microphysical processes. In this simulation this characteristic time scale varies slowly within the population, similar to what might be expected in a weakly forced, quasi-uniform environment like the tropical oceans. Indeed, Shige (1999) observed a persistent gravity wave signal in the tropics with 1-h period that lasted approximately 6 h. Thus, it is reasonable to assume that the characteristic convective time scale plays a governing role in defining the frequency peaks in the gravity wave spectra.

In this case, the convection preferentially couples to the $n = 3$ gravity wave modes with periods matching characteristic convective time scales of approximately 1 and 2 h (Fig. 5). For a wave period of 2 h the $n = 3$ mode has a horizontal wavelength of about 110 km and for a period of 1 h it would have a horizontal wavelength of approximately 50 km (Fig. 12). These horizontal wavelengths far exceed the width of individual cloud systems (cf. Figs. 6 and 9) yet encompass the emergent spacing of those systems. This result implies that the cloud systems are only present at the peaks of the tropospheric waves and not within their entire upward phase. For a given vertical wavelength, longer wave periods lead to longer wavelength waves, and, if coupled to the cloud population, would lead to larger cloud-system spacing. The similarity in the depth and characteristic convective time scales among cloud systems within active regions of the cloud population ensures that the waves will be sufficiently similar, which is an ingredient that enables interference between waves propagating in opposite horizontal directions.

To further demonstrate the influence of changes in the characteristic time scale on the generated gravity waves, two idealized dry simulations are conducted. Each of these simulations is forced by a periodic (in time) diabatic heat source designed to approximate a transient

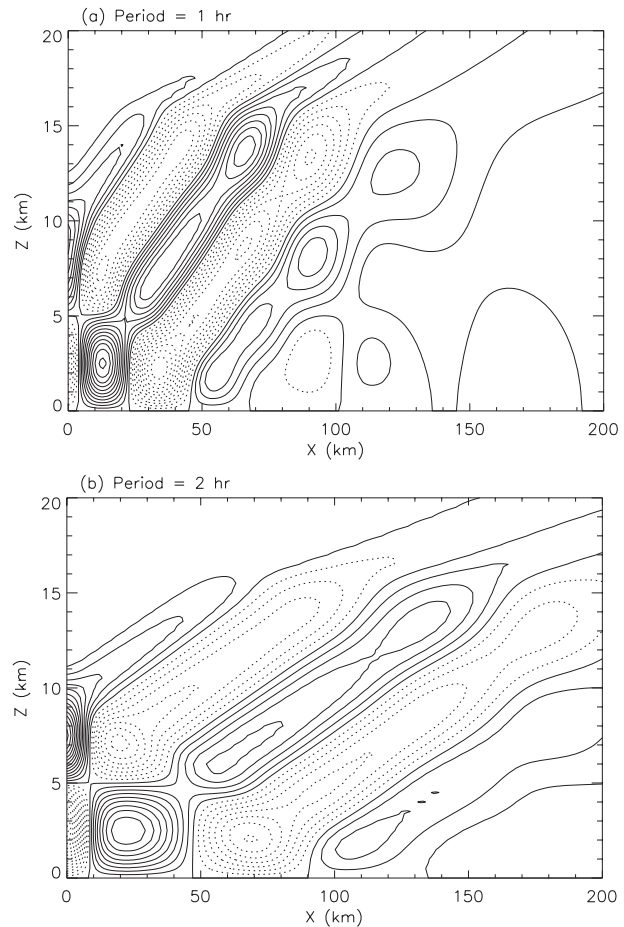


FIG. 13. Vertical velocity from the idealized dry simulations with source periods equal to (a) 1 and (b) 2 h. Contour interval is 0.05 m s^{-1} , negative contours are dashed, and the time is (a) 8000 and (b) 16 000 s after initialization.

source with similar spatial dimensions to the convective systems in the population. The source is approximately 20 km wide, 10 km deep, and with a sinusoidal vertical wavelength equal to this depth (akin to *stratiform heating*); see the appendix for details. Figure 13 shows the vertical velocity for sources with periods equal to (Fig. 13a) 1 h and (Fig. 13b) 2 h; both images are valid after approximately two source periods. Both Figs. 13a and 13b demonstrate the notable wave response in the troposphere; in both cases the waves possess an $n = 3$ vertical structure, resulting from a combination of the depth of the source and its projection onto this vertical harmonic of the troposphere. The horizontal wavelengths of these waves are in agreement with the aforementioned discussion, namely, approximately 50 km for the source with 1-h period and 100 km for the source with 2-h period. Admittedly, this idealized source configuration is an oversimplification of the dynamics underlying the convection modeled in the CSRM. Yet, these results clearly

demonstrate the ability of a localized source—analogous to the convective elements embedded within the cloud systems—to generate tropospheric gravity waves with horizontal wavelengths much larger than the width of the source. Moreover, these experiments also show that, for these source dimensions, a periodic source that spans two-thirds of the tropospheric depth projects efficiently onto the $n = 3$ mode. Although not shown here, this result can also be derived using a similar analysis to that conducted by Holton et al. (2002).

e. Other gravity wave–cloud interactions

As discussed above, the coupling between the cloud population and the $n = 3$ modes plays an important role in determining the emergent spacing of the evolving cloud population. In addition, the gravity waves appear to interact with the mesoscale cloud systems in at least two other ways.

The first process relates to the initiation of convection. For example, in Figs. 11a and 11c an active convective system is present immediately preceding subsidence region S1. The gravity waves emanating from this system (marked on the figure with lines) link directly to the initiation of cells A2 and B2. This is a similar pattern identified by numerous other authors on a variety of scales (e.g., Numaguti and Hayashi 2000; Peng et al. 2001; Tulich and Mapes 2008). Such initiation could be entirely associated with the $n = 3$ modes, or (more likely) the different tropospheric wave modes (e.g., $n = 1, 2$, and 3) generated by the parent convective system could interfere to promote convective development some distance from the original source (e.g., McAnelly et al. 1997). In this specific case, the initiation of A2 and B2 occurs at the preferred spacing for resonance to occur between the cloud systems and the $n = 3$ modes. The amplification of the $n = 3$ gravity wave accompanies the initiation of these two cells (Fig. 10), perhaps also leading to the demise of the parent storm through enhanced subsidence at S1. Nonetheless, the initiation of cloud systems at the preferred spacing does not account for all occurrences of convective initiation, and Fig. 1 suggests that in many cases the large-scale propagating structures also play a role in initiating the cloud systems. Furthermore, such initiation is not essential for the gravity wave–convection coupling to occur; the preferential development of cloud systems spaced one wavelength apart could emerge from a randomly spaced cloud population, or within one of the broader regions of preferred convective activity.

The second process relates to the role of the gravity waves in promoting the longevity of mesoscale cloud systems. For example, both A2 and B2 last for approximately 10 h after initiation. Throughout this system

lifetime numerous bursts of convective activity occur, each with a characteristic convective time scale of 1–2 h. Many of these bursts appear related to the arrival of a gravity wave that propagates from the neighboring system; a few of these are marked in Figs. 11a and 11c as lines stretching from one system to the other. Indeed, it appears that the neighboring convective systems form a collaborative relationship, with propagating gravity waves providing the mechanism for renewed convective activity and system longevity. Such longevity is in agreement with the two time scales identified earlier from Fig. 5: the characteristic convective time scale and the mesoscale cloud-system lifetime.

Finally, note that the drift of the mesoscale cloud systems in Fig. 11 is only 1–2 m s⁻¹. This approximately corresponds to the mean low-level wind in the region of active convection, which is probably related to the local variations of the horizontal flow associated with the passage of large-scale propagating structures. The movement of these systems appears to be similar to propagating structures found in large-scale convectively coupled waves that have been attributed to inertia–gravity waves (e.g., Fig. 15 of Numaguti and Hayashi 2000).

3. Summary

An idealized cloud-system-resolving model (CSRM) simulation was used to demonstrate evidence of coupling between a cloud population and the mesoscale gravity waves it generated. This coupling is manifest as the emergence of quasi-regular cloud-system spacing within the evolving population as it became self-organized. Gravity waves also played a role in the initiation and longevity of mesoscale cloud systems, a process that worked alongside the formation of the other larger-scale propagating structures similar to larger-scale convectively coupled waves.

A notable characteristic of the cloud population was cloud systems with a 2-h convective life cycle and approximately 100-km horizontal spacing. Spectral analysis of the cloud field demonstrated a coherent signal along a line in spectral space that corresponded to the quotient of the cloud spacing and the characteristic convective time scale equal to approximately 13 m s⁻¹. This cloud signal overlapped in spectral space with an enhanced gravity wave with a vertical wavelength of approximately two-thirds of the tropospheric depth, namely, the $n = 3$ mode. The coupling between this wave and the cloud population emerged at specific time scales, corresponding to the characteristic convective time scale of the structures embedded within the longer-lived cloud systems. The convective time scale, along with the vertical wavelength of the $n = 3$ gravity wave, determined the

horizontal wavelength of the wave through constraints placed by the dispersion relation; this horizontal wavelength matched the spacing of mesoscale cloud systems.

Examination of the CSRM cloud and wave distribution demonstrated that the cloud systems did indeed become coupled to the $n = 3$ gravity wave field, which forms in part due to partial reflection of the waves by the tropopause. The approximate symmetry in the wave field supported the interaction of gravity waves propagating in opposing horizontal directions, which were generated by adjacent or distant wave sources. Such interactions allowed the temporary formation of horizontal standing waves, facilitating localized resonance between the cloud population and the wave field. Convective development approximately coincided with the upward phase of the $n = 3$ wave near the surface and suppression of clouds in the downward phase. During these interactions the clouds themselves did not propagate at the gravity wave speeds but remained almost stationary.

Of course, the cloud and wave fields were intertwined in the modeled population, making it difficult to isolate cause and effect. Yet, examination of the clouds and the tropospheric vertical velocity (e.g., Fig. 11) clearly showed that individual clouds were responsible for generating the waves with horizontal wavelengths of order 100 km; the idealized dry model showed similar generation as well. This property of the wave source removes some of the ambiguity regarding the origin of the horizontal scale, and suggests that the gravity waves with horizontal wavelengths of order 100 km were not the result of the spacing of the cloud systems, but the original cause of that spacing. Once the cloud-system spacing is established, however, amplification of the wave spectrum at those horizontal scales is likely.

Robinson et al. (2008) also highlighted the importance of the gravity wave dispersion relation and characteristic temporal and height scales in constraining the horizontal wavelength. They described an optimum situation for convective development based on the size of surface “hot spots” such as islands, arguing that a resonance could occur if the spatial and temporal scale of the forcing were related in the same way as defined by the dispersion relation. Unlike the argument presented herein, their vertical scale was related to the depth of the boundary layer instead of the depth of a gravity wave mode. In these CSRM simulations, localized forcing can only arise from cloud-induced circulations like gust fronts and gravity waves. By definition, the rich gravity wave spectrum generated by the cloud population must satisfy the Robinson et al. optimum conditions everywhere, yet does not take the form of external forcing like an island.

This work has focused on an idealized scenario, featuring two-dimensional geometry and an unsheared basic state. Two-dimensional geometry would maximize wave interactions at distances remote from the wave source and further investigations of these processes in three dimensions are continuing. In three dimensions the coupling may only occur in special cases, such as in cloud populations with convective systems that have large horizontal aspect ratios that mimic two-dimensional geometry. Finally, the inclusion of wind shear would produce a directional bias to the wave field (e.g., Stechmann and Majda 2009), perhaps resulting in a coupling that is manifest with propagating systems instead of the quasi-stationary systems considered herein.

Acknowledgments. TPL acknowledges support from the Australian Research Council Discovery Projects (DP0770381) and Future Fellowships (FT0990892) Schemes. FZ acknowledges support from National Science Foundation Grants ATM-0618662 and ATM-0904635. We are grateful to Craig Epifanio and Mitch Moncrieff for helpful discussions and to the editor (Prof. Yoden) and three anonymous reviewers for their thorough reviews that helped improve the manuscript.

APPENDIX

Configuration of Dry Simulations

This appendix describes the formulation of the idealized dry simulations used to create Fig. 13. The model is a finite difference approximation to the dry two-dimensional Boussinesq equations of motion:

$$\begin{aligned} \frac{\partial u}{\partial t} + u \frac{\partial u}{\partial x} + w \frac{\partial u}{\partial z} &= -\frac{1}{\rho_*} \frac{\partial p}{\partial x}, \\ \frac{\partial w}{\partial t} + u \frac{\partial w}{\partial x} + w \frac{\partial w}{\partial z} &= -\frac{1}{\rho_*} \frac{\partial p}{\partial z} + b, \\ \frac{\partial b}{\partial t} + u \frac{\partial b}{\partial x} + w \frac{\partial b}{\partial z} + w N^2 &= \frac{g}{\theta_*} Q, \quad \text{and} \\ \frac{\partial u}{\partial x} + \frac{\partial w}{\partial z} &= 0 \end{aligned}$$

in which u is the horizontal velocity, w the vertical velocity, b the buoyancy, p the perturbation pressure, and Q is the diabatic forcing; $\theta_* = 300$ K, $g = 9.8$ m s $^{-2}$, and $\rho_* = 1$ kg m $^{-3}$. The numerical formulation of this model is described in Lane (2008). The model domain is 1000 km wide and 35 km high with horizontal and vertical grid spacing of

1 km and 500 m, respectively; the time step is 20 s. Rayleigh damping is used to mitigate wave reflections off the model's lateral and uppermost boundaries; the lateral damping regions are each 200 km wide and the upper absorber is 15 km deep. The Brunt–Väisälä frequency is equal to 9×10^{-3} rad s $^{-1}$ below 16 km and 2.2×10^{-2} rad s $^{-1}$ above 16 km, similar to the average tropospheric and stratospheric values in the CSRM.

The spatial structure of the diabatic forcing is of the form

$$q(x, z) = \begin{cases} Q_0 \exp(-x^2/\sigma^2) \sin(2\pi z/H), & 0 \leq z \leq H \\ 0, & z > H, \end{cases}$$

where $H = 10$ km is the forcing depth and $\sigma = 10$ km is the forcing half-width. The forcing is periodic in time such that

$$Q = -\frac{2\theta_0}{g} q(x, z) \sin(\omega t)$$

in which ω is the source frequency. The fluid is initially at rest and gravity waves are generated by imposing the forcing, Q , at the horizontal center of the model domain. While the full nonlinear equations are used, the amplitude of the forcing is sufficiently small ($Q_0 = 10^{-3}$ K day $^{-1}$) that a linear wave response should be expected (see, e.g., Pandya and Alexander 1999). While the wave amplitudes are not particularly relevant from this quasi-linear calculation, they are multiplied by a factor of 2×10^5 to illustrate the equivalent linear response to a forcing with amplitude of ~ 8 K h $^{-1}$.

REFERENCES

- Balaji, V., and T. L. Clark, 1988: Scale selection in locally forced convective fields and the initiation of deep cumulus. *J. Atmos. Sci.*, **45**, 3189–3211.
- , J.-L. Redelsperger, and G. P. Klaassen, 1993: Mechanisms for the mesoscale organization of tropical cloud clusters in GATE Phase III. Part I: Shallow cloud bands. *J. Atmos. Sci.*, **50**, 3571–3589.
- Bretherton, C. S., and P. K. Smolarkiewicz, 1989: Gravity waves, compensating subsidence, and detrainment around cumulus clouds. *J. Atmos. Sci.*, **46**, 740–759.
- Bretherton, F. P., 1966: The propagation of groups of internal gravity waves in a shear flow. *Quart. J. Roy. Meteor. Soc.*, **92**, 466–480.
- Bruunjes, R. T., T. L. Clark, and W. D. Hall, 1994: Interactions between topographic airflow and cloud/precipitation development during the passage of a winter storm in Arizona. *J. Atmos. Sci.*, **51**, 48–67.
- Chagnon, J. M., 2010: Gravity waves, dynamical resistance, and forcing efficiency. *J. Atmos. Sci.*, **67**, 2039–2051.
- Clark, T. L., 1977: A small-scale dynamic model using a terrain-following coordinate transformation. *J. Comput. Phys.*, **24**, 186–215.
- , W. D. Hall, and J. L. Coen, 1996: Source code documentation for the Clark-Hall cloudscale model: Code version G3CH01. NCAR Tech. Note NCAR/TN-426+STR, 137 pp.
- Cohen, B. G., and G. C. Craig, 2004: The response time of a convective cloud ensemble to a change in forcing. *Quart. J. Roy. Meteor. Soc.*, **130**, 933–944.
- Fovell, R. G., 2002: Upstream influence of numerically simulated squall-lines. *Quart. J. Roy. Meteor. Soc.*, **128**, 893–912.
- Fritts, D. C., and M. J. Alexander, 2003: Gravity wave dynamics and effects in the middle atmosphere. *Rev. Geophys.*, **41**, 1003, doi:10.1029/2001RG000106.
- Halverson, J. B., B. S. Ferrier, T. M. Rickenbach, J. Simpson, and W.-K. Tao, 1999: An ensemble of convective systems on 11 February 1993 during TOGA COARE: Morphology, rainfall characteristics, and anvil cloud interactions. *Mon. Wea. Rev.*, **127**, 1208–1228.
- Holton, J. R., J. H. Beres, and X. Zhou, 2002: On the vertical scale of gravity waves excited by localized thermal forcing. *J. Atmos. Sci.*, **59**, 2019–2023.
- Kessler, E., 1969: *On the Distribution and Continuity of Water Substance in Atmospheric Circulations*. Meteor. Monogr., No. 32, Amer. Meteor. Soc., 84 pp.
- Kiladis, G. N., M. C. Wheeler, P. T. Haertel, K. H. Straub, and P. E. Roundy, 2009: Convectively coupled equatorial waves. *Rev. Geophys.*, **47**, RG0003, doi:10.1029/2008RG000266.
- Kim, Y.-J., S. D. Eckermann, and H.-Y. Chun, 2003: An overview of past, present and future of gravity-wave drag parametrization for numerical climate and weather prediction models. *Atmos.–Ocean*, **41**, 65–98.
- Koch, S. E., F. Zhang, M. L. Kaplan, Y.-L. Lin, R. Weglarz, and C. M. Trexler, 2001: Numerical simulation of a gravity wave event observed during CCOPE. Part III: Mountain–plain solenoids in the generation of the second wave episode. *Mon. Wea. Rev.*, **129**, 909–932.
- Koenig, L. R., and F. W. Murray, 1976: Ice-bearing cumulus cloud evolution: Numerical simulation and general comparison against observations. *J. Appl. Meteor.*, **15**, 747–762.
- Küpper, C., J. Thuburn, G. C. Craig, and T. Birner, 2004: Mass and water transport into the tropical stratosphere: A cloud-resolving simulation. *J. Geophys. Res.*, **109**, D10111, doi:10.1029/2004JD004541.
- Lac, C., J.-P. Lafore, and J.-L. Redelsperger, 2002: Role of gravity waves in triggering deep convection during TOGA-COARE. *J. Atmos. Sci.*, **59**, 1293–1316.
- Lane, T. P., 2008: The vortical response to penetrative convection and the associated gravity wave generation. *Atmos. Sci. Lett.*, **9**, 103–110.
- , and M. J. Reeder, 2001: Convectively generated gravity waves and their effect on the cloud environment. *J. Atmos. Sci.*, **58**, 2427–2440.
- , and M. W. Moncrieff, 2008: Stratospheric gravity waves generated by multiscale tropical convection. *J. Atmos. Sci.*, **65**, 2598–2614.
- , and —, 2010: Characterization of momentum transport associated with organized moist convection and gravity waves. *J. Atmos. Sci.*, **67**, 3208–3225.
- , M. J. Reeder, and T. L. Clark, 2001: Numerical modeling of gravity wave generation by deep tropical convection. *J. Atmos. Sci.*, **58**, 1249–1274.
- Lindzen, R. S., 1974: Wave-CISK in the tropics. *J. Atmos. Sci.*, **31**, 156–179.
- , and K.-K. Tung, 1976: Banded convective activity and ducted gravity waves. *Mon. Wea. Rev.*, **104**, 1602–1617.
- Liu, C., and M. W. Moncrieff, 2004: Effects of convectively generated gravity waves and rotation on the organization of convection. *J. Atmos. Sci.*, **61**, 2218–2227.

- Mapes, B. E., 1993: Gregarious tropical convection. *J. Atmos. Sci.*, **50**, 2026–2037.
- Marsham, J. H., and D. J. Parker, 2006: Secondary initiation of multiple bands of cumulonimbus over southern Britain. II: Dynamics of secondary initiation. *Quart. J. Roy. Meteor. Soc.*, **132**, 1053–1072.
- McAnelly, R. L., J. E. Nachamkin, W. R. Cotton, and M. E. Nicholls, 1997: Upscale evolution of MCSs: Doppler radar analysis and analytical investigation. *Mon. Wea. Rev.*, **125**, 1083–1110.
- Monserrat, S., and A. J. Thorpe, 1996: Use of ducting theory in an observed case of gravity waves. *J. Atmos. Sci.*, **53**, 1724–1736.
- Morcrette, C. J., K. A. Browning, A. M. Blyth, K. E. Bozier, P. A. Clark, D. Ladd, E. G. Norton, and E. Pavelin, 2006: Secondary initiation of multiple bands of cumulonimbus over southern Britain. I: An observational case-study. *Quart. J. Roy. Meteor. Soc.*, **132**, 1021–1051.
- Nehrkorn, T., 1986: Wave-CISK in a baroclinic basic state. *J. Atmos. Sci.*, **43**, 2773–2791.
- Nicholls, M. E., R. A. Pielke, and W. R. Cotton, 1991: Thermally forced gravity waves in an atmosphere at rest. *J. Atmos. Sci.*, **48**, 1869–1884.
- Numaguti, A., and Y. Hayashi, 2000: Gravity-wave dynamics of the hierarchical structure of super cloud clusters. *J. Meteor. Soc. Japan*, **78**, 301–331.
- Oouchi, K., 1999: Hierarchical organization of super cloud cluster caused by WISHE, convectively induced gravity wave and cold pool, 1999. *J. Meteor. Soc. Japan*, **77**, 907–927.
- Pandya, R. E., and M. J. Alexander, 1999: Linear stratospheric gravity waves above convective thermal forcing. *J. Atmos. Sci.*, **56**, 2434–2446.
- , D. R. Durran, and M. L. Weisman, 2000: The influence of convective thermal forcing on the three-dimensional circulation around squall lines. *J. Atmos. Sci.*, **57**, 29–45.
- Peng, L., C.-H. Sui, K.-M. Lau, and W.-K. Tao, 2001: Genesis and evolution of hierarchical cloud clusters in a two-dimensional cumulus-resolving model. *J. Atmos. Sci.*, **58**, 877–895.
- Pessi, A. T., and S. Businger, 2009: Relationships among lightning, precipitation, and hydrometeor characteristics over the North Pacific Ocean. *J. Appl. Meteor. Climatol.*, **48**, 833–848.
- Powers, J. G. and R. J. Reed, 1993: Numerical simulation of the large-amplitude mesoscale gravity-wave event of 15 December 1987 in the central United States. *Mon. Wea. Rev.*, **121**, 2285–2308.
- Raymond, D. J., 1987: A forced gravity wave model of self-organizing convection. *J. Atmos. Sci.*, **44**, 3528–3543.
- Robinson, F. J., S. C. Sherwood, and Y. Li, 2008: Resonant response of deep convection to surface hot spots. *J. Atmos. Sci.*, **65**, 276–286.
- Schmidt, J. M., and W. R. Cotton, 1990: Interactions between upper and lower tropospheric gravity waves on squall line structure and maintenance. *J. Atmos. Sci.*, **47**, 1205–1222.
- Shige, S., 1999: Disturbances of 1–2 hour periods observed in the tropical lower troposphere during the TOGA-COARE IOP. *J. Meteor. Soc. Japan*, **77**, 1123–1136.
- , and T. Satomura, 2000: The gravity wave response in the troposphere around deep convection. *J. Meteor. Soc. Japan*, **78**, 789–801.
- , and —, 2001: Westward generation of eastward-moving tropical convective bands in TOGA COARE. *J. Atmos. Sci.*, **58**, 3724–3740.
- Song, I.-S., H.-Y. Chun, and T. P. Lane, 2003: Generation mechanisms of convectively forced internal gravity waves and their propagation to the stratosphere. *J. Atmos. Sci.*, **60**, 1960–1980.
- Stechmann, S. N., and A. J. Majda, 2009: Gravity waves in shear and implications for organized convection. *J. Atmos. Sci.*, **66**, 2579–2599.
- Tompkins, A. M., and G. C. Craig, 1998: Radiative–convective equilibrium in a three-dimensional cloud-ensemble model. *Quart. J. Roy. Meteor. Soc.*, **124**, 2073–2097.
- Tulich, S. N., and B. E. Mapes, 2008: Multiscale convective wave disturbances in the tropics: Insights from a two-dimensional cloud-resolving model. *J. Atmos. Sci.*, **65**, 140–155.
- , D. A. Randall, and B. E. Mapes, 2007: Vertical-mode and cloud decomposition of large-scale convectively coupled gravity waves in a two-dimensional cloud resolving model. *J. Atmos. Sci.*, **64**, 1210–1229.
- Wheeler, M., and G. N. Kiladis, 1999: Convectively coupled equatorial waves: Analysis of clouds and temperature in the wavenumber–frequency domain. *J. Atmos. Sci.*, **56**, 374–399.
- Yanai, M., S. Esbensen, and J.-H. Chu, 1973: Determination of bulk properties of tropical cloud clusters from large-scale heat and moisture budgets. *J. Atmos. Sci.*, **30**, 611–627.
- Zhang, F., S. E. Koch, C. A. Davis, and M. L. Kaplan, 2001: Wavelet analysis and the governing dynamics of a large-amplitude gravity wave event along the East Coast of the United States. *Quart. J. Roy. Meteor. Soc.*, **127**, 2209–2245.